Transmission and information encryption of windmill array beams in oceanic turbulence

Jun-Hao Xu(许俊豪), Yu-Qing Zhao(赵宇晴), Fa-Jing Li(李发静), Cao-Jin Yuan(袁操今)
Citation: Chin. Phys. B. 35, 104204 (2026). DOI: 10.1088/1674-1056/ae64d0 | CSTR: 32038.14.CPB.ae64d0
http://cpb.iphy.ac.cn; http://iopscience.iop.org/cpb

What follows is a list of articles you may be interested in

Optical design of the time-resolved ARPES beamline of the new material spectroscopy experimental station for the update of CAEP THz-FEL facility

Liang-Liang Du(杜亮亮), Li-Min Meng(孟立民), Jiang Li(李江), Li-Guo Zhu(朱礼国)
Chin. Phys. B. 33, 114203 (2024). DOI: 10.1088/1674-1056/ad73b1

Topological resonators based on hexagonal-star valley photonic crystals

Xin Wan(万鑫), Chenyang Peng(彭晨阳), Gang Li(李港), Junhao Yang(杨俊豪), Xinyuan Qi(齐新元)
Chin. Phys. B. 32, 114208 (2023). DOI: 10.1088/1674-1056/acf44b

High-performance chiral all-optical OR logic gate based on topological edge states of valley photonic crystal

Xiaorong Wang(王晓蓉), Hongming Fei(费宏明), Han Lin(林瀚), Min Wu(武敏), Lijuan Kang(康丽娟), Mingda Zhang(张明达), Xin Liu(刘欣), Yibiao Yang(杨毅彪), Liantuan Xiao(肖连团)
Chin. Phys. B. 32, 074205 (2023). DOI: 10.1088/1674-1056/accb41

Modulated spatial transmission signals in the photonic bandgap

Wenqi Xu(许文琪), Hui Wang(王慧), Daohong Xie(谢道鸿), Junling Che(车俊岭), Yanpeng Zhang(张彦鹏)
Chin. Phys. B. 31, 124209 (2022). DOI: 10.1088/1674-1056/ac76b3

Dynamically tunable multiband plasmon-induced transparency effect based on graphene nanoribbon waveguide coupled with rectangle cavities system

Zi-Hao Zhu(朱子豪), Bo-Yun Wang(王波云), Xiang Yan(闫香), Yang Liu(刘洋), Qing-Dong Zeng(曾庆栋), Tao Wang(王涛), Hua-Qing Yu(余华清)
Chin. Phys. B. 31, 084210 (2022). DOI: 10.1088/1674-1056/ac7e39

Transmission and information encryption of windmill array beams in oceanic turbulence

Jun-Hao Xu(许俊豪), Yu-Qing Zhao(赵宇晴), Fa-Jing Li(李发静)[†], and Cao-Jin Yuan(袁操今)[‡]

School of Physics and Technology, Nanjing Normal University, Nanjing 210023, *China*

(Received 4 February 2026; revised manuscript received 25 March 2026; accepted manuscript online 27 April 2026)

Oceanic turbulence-induced beam wandering, scintillation and phase distortion are the main factors limiting underwater optical communication performance. To address this issue, this study investigates the propagation of windmill array beams through oceanic turbulence and evaluates their potential application as binary information carriers. A cross-spectral density evolution model based on the extended Huygens–Fresnel principle and Nikishov's temperature–salinity spectrum is employed to analyze the propagation characteristics of windmill beams in oceanic turbulence. Numerical simulation results suggest that windmill beams can preserve their basic structure during propagation in oceanic turbulence. Furthermore, laboratory experiments conducted in a 1.2 m turbulence simulator demonstrate that windmill beams preserve stable and distinguishable leaf structures under pump-induced turbulence and varying salinity levels. Since the number of leaves remains constant at different propagation distances, we further propose an effective encoding scheme mapping leaf number 1–4 to 2-bit symbols, combined with convolutional neural network (CNN) decoding. Experimental results demonstrate that the system, integrated with CNN-based decoding, maintains high recognition accuracy despite turbulence-induced distortions. The CNN-based decoder consistently achieves classification confidence above 98.0% under turbulent conditions and salinity levels ranging from 0 to 3.3%. These findings suggest windmill beams as a promising approach to enhance reliability and capacity in underwater optical communication.

Keywords: structured light transmission, windmill beams, CNN-based decoding, underwater optical communication

PACS: 42.25.Bs, 42.60.Jf, 42.68.–w

DOI: 10.1088/1674-1056/ae64d0 **CSTR:** 32038.14.CPB.ae64d0

1. Introduction

In recent years, underwater wireless optical communication (UWOC) has demonstrated immense potential application in marine exploration, underwater sensor networks, and real-time video transmission due to its wide bandwidth, high data rates, low latency, and robust security.[1–3] However, the complex marine environment poses significant challenges to optical signal transmission. Among these, oceanic turbulence induces random fluctuations in refractive index, leading to beam speckle drift, intensity flicker, and phase distortion, which severely limit communication quality.[4–6]

To overcome these effects, structured beams with unique spatial configurations and orbital angular momentum (OAM), such as Laguerre–Gaussian beams, Bessel beams, and other vortex beams, have become a research focus.[7–11] Existing studies have investigated the evolution of various structured beams in oceanic turbulence, including partially coherent circularly polarized vortex beams,[12] Laguerre–Gaussian beams,[4,13,14] partially coherent radially polarized off-axis double vortex beams,[15] Bessel–Gaussian beams,[16] Airy vortex beams[17] and rotationally symmetric power-exponential phase vortex beams.[18] Additionally, studies on multi-Gaussian correlated anomalous hollow beams[19] and power-exponent-phase vortex beams[20] have further expanded the theoretical framework for complex beam propagation in underwater environments. These studies demonstrate that modulating the beam's phase,[18,20,21] coherence,[5,19] or polarization state[12,22] can effectively enhance robustness in turbulent environments, while offering new degrees of freedom for increasing underwater communication capacity.

In recent research, Niu *et al*. proposed a rotating windmill array beam with adjustable wing angles. Furthermore, they employed a phase rotation superposition method to construct windmill array beams with varying leaf numbers. The results show that the windmill beam exhibits self-rotating and self-bending characteristics during propagation.[23,24] Besides that, the number of its leaves remains constant and clearly distinguishable at different propagation distances, which indicates that this type of beam has potential applications in information transmission.

Although the characteristics of windmill beams in free space have been preliminarily investigated, their behaviors within more complex random media — such as oceanic turbulence — remain unknown. The propagation of windmill beams, with discrete leaves and tunable geometric parameters, under Nikishov's combined temperature–salinity contribution

[†]Corresponding author. E-mail: 90960@njnu.edu.cn

[‡]Corresponding author. E-mail: yuancj@njnu.edu.cn

© 2026 Chinese Physical Society and IOP Publishing Ltd. All rights, including for text and data mining, AI training, and similar technologies, are reserved.

ocean spectrum[6] has yet to be systematically elucidated.

In this paper, we characterize the propagation of windmill beams through oceanic turbulence for underwater optical communication. We employ a cross-spectral density (CSD) evolution model based on the extended Huygens–Fresnel (EHF) principle and Nikishov's spectrum. Both numerical simulations and experiments demonstrate that the fundamental leaf structure of windmill beams maintains stability during underwater propagation. Furthermore, we explore the reliability of these beams as binary information carriers for the first time. We conduct experimental investigations and employ a CNN to enhance the decoding efficiency. The experimental results show that these beams achieve high decoding accuracy in oceanic turbulent environments, which validates the feasibility of the encoding and decoding scheme based on windmill array beams.

2. Theoretical model

In this work, the windmill beam is generated by a Gaussian beam passing through a specific phase modulation. The complex amplitude of the beam at the initial plane ($z=0$) can be expressed as[23,24]

$$E(r,\phi,0)=E_0\exp\left(-\frac{r^2}{w_0^2}\right)\exp[\mathrm{i}a\cdot r^b\cdot\beta], \tag{1}$$

where r and ϕ are polar coordinates at the source plane, E_0 is a constant amplitude, which is set as 1 for convenience, w_0 is the beam waist radius of the fundamental Gaussian envelope, a represents the stretching extent and r^b is a power term of the radial coordinate. In Cartesian coordinates, the azimuth angle ϕ is expressed as follows:

$$\phi=\operatorname{atan}2(y,x), \tag{2}$$

where atan2 function computes the polar angle of the vector (x, y) measured from the positive x-axis. Its output lies in the range $(-\pi,\pi]$. To represent the phase variation over the range $(-\pi,\pi]$ as an elliptical distribution, the azimuthal angle β is defined as

$$\begin{aligned}&\beta=\operatorname{atan}2\left(\frac{y}{\sin\alpha},\frac{x}{\cos\alpha}\right),\\&(x,y)=(r\cos\phi,r\sin\phi).\end{aligned} \tag{3}$$

Here, α denotes the ellipticity of the windmill beam coordinate distribution. β is a phase-mapping angle used only to construct the windmill phase term in Eq. (1).

To describe the propagation of structured beams through oceanic turbulence, we employ the extended Huygens–Fresnel principle together with the oceanic turbulence spectrum.[25] Following the unified theory of coherence and polarization,[26] beam propagation is characterized by the cross-spectral density (CSD), which is defined between two arbitrary transverse points. We consider two transverse planes: the source plane at $z=0$ and the receiving plane at $z>0$. At the source plane, the two points are denoted by (r_1,ϕ_1) and (r_2,ϕ_2), with the corresponding Cartesian coordinates (x_1,y_1) and (x_2,y_2). At the receiving plane, the two points are denoted by (ρ_1,θ_1) and (ρ_2,θ_2). ϕ denotes the physical azimuth angle used in the following propagation kernel and the integration measurement, while β appears only in the source phase term.

Accordingly, the cross-spectral density at the source plane ($z=0$) can be written as

$$\begin{aligned}&W(r_1,r_2,\phi_1,\phi_2,0)=\langle E(r_1,\phi_1)E^*(r_2,\phi_2)\rangle\\&=\exp\left(-\frac{r_1^2+r_2^2}{w_0^2}\right)\exp\left[\mathrm{i}a\left(r_1^b\beta_1-r_2^b\beta_2\right)\right],\end{aligned} \tag{4}$$

where

$$\begin{aligned}&\beta_i=\operatorname{atan}2\left(\frac{y_i}{\sin\alpha},\frac{x_i}{\cos\alpha}\right),\quad i=1,2,\\&(x_i,y_i)=(r_i\cos\phi_i,r_i\sin\phi_i).\end{aligned} \tag{5}$$

The symbols '*' and '$\langle\,\rangle$' represent the complex conjugate and the ensemble average over the turbulent medium, respectively.

The extended Huygens–Fresnel principle is widely used to describe beam propagation through turbulence.[6] Accordingly, the cross-spectral density (CSD) of the windmill beam propagating through oceanic turbulence at a receiving plane ($z>0$) can be expressed as follows:[18]

$$\begin{aligned}&W(\rho_1,\rho_2,\theta_1,\theta_2,z)\\&=\left(\frac{k}{2\pi z}\right)^2\int_0^{+\infty}\int_0^{+\infty}\int_0^{2\pi}\int_0^{2\pi}W(r_1,r_2,\phi_1,\phi_2,0)\\&\times\exp\left[-\frac{\mathrm{i}k}{2z}\left(\rho_1^2-2r_1\rho_1\cos(\phi_1-\theta_1)+r_1^2\right)\right]\\&\times\exp\left[\frac{\mathrm{i}k}{2z}\left(\rho_2^2-2r_2\rho_2\cos(\phi_2-\theta_2)+r_2^2\right)\right]\\&\times\langle\exp[\psi(\boldsymbol{\rho}_1,\boldsymbol{r}_1)+\psi^*(\boldsymbol{\rho}_2,\boldsymbol{r}_2)]\rangle r_1r_2\,\mathrm{d}r_1\,\mathrm{d}r_2\,\mathrm{d}\phi_1\,\mathrm{d}\phi_2.\end{aligned} \tag{6}$$

Here, θ_1 and θ_2 denote the polar angles at the receiving plane. The wavenumber is defined as $k=2\pi/\lambda$, where λ is the wavelength. $\boldsymbol{\rho}_1$ and $\boldsymbol{\rho}_2$ represent the position vectors at the receiving plane, and $\boldsymbol{r}_1$ and $\boldsymbol{r}_2$ represent the position vectors at the source plane. The term $\psi(\boldsymbol{\rho}_i,\boldsymbol{r}_i)$ ($i=1,2$) denotes the random component of the complex phase of spherical wave induced by turbulence. The ensemble average over the oceanic turbulence is expressed as[19]

$$\begin{aligned}&\langle\exp[\psi(\boldsymbol{\rho}_1,\boldsymbol{r}_1)+\psi^*(\boldsymbol{\rho}_2,\boldsymbol{r}_2)]\rangle\\&=\exp\left\{-\frac{\pi^2k^2z}{3}\int_0^{\infty}\mathrm{d}\kappa\kappa^3\Phi(\kappa)[(\boldsymbol{\rho}_1-\boldsymbol{\rho}_2)^2\right.\\&\left.+(\boldsymbol{r}_1-\boldsymbol{r}_2)(\boldsymbol{\rho}_1-\boldsymbol{\rho}_2)+(\boldsymbol{r}_1-\boldsymbol{r}_2)^2]\right\},\end{aligned} \tag{7}$$

where $\boldsymbol{\kappa}$ denotes the spatial frequency. $\Phi(\kappa)$ represents the spatial power spectrum of the refractive index fluctuations in oceanic turbulence, expressed as

$$\Phi(\kappa)=0.388\times10^{-8}\varepsilon^{-1/3}\kappa^{-11/3}$$

$$\times \frac{\chi_{\mathrm{T}}}{\omega^2}\left[1+2.35(\kappa\eta)^{2/3}\right] \times \left(\omega^2 \mathrm{e}^{-A_{\mathrm{T}}\delta}+\mathrm{e}^{-A_{\mathrm{S}}\delta}-2\omega \mathrm{e}^{-A_{\mathrm{TS}}\delta}\right). \quad (8)$$

The strength of oceanic turbulence can be written as

$$\begin{aligned} G &= \frac{\pi^2}{3}\int_0^{\infty} \kappa^3 \Phi(\kappa)\mathrm{d}\kappa \\ &= \frac{\pi^2}{3}\int_0^{\infty} \kappa^3 0.388\times 10^{-8}\mathrm{e}^{-1/3}\kappa^{-11/3}\frac{\chi_{\mathrm{T}}}{\omega^2} \\ &\quad \times\left[1+2.35(\kappa\eta)^{2/3}\right] \\ &\quad \times\left(\omega^2 \mathrm{e}^{-A_{\mathrm{T}}\delta}+\mathrm{e}^{-A_{\mathrm{S}}\delta}-2\omega \mathrm{e}^{-A_{\mathrm{TS}}\delta}\right)\mathrm{d}\kappa, \end{aligned} \quad (9)$$

where $\delta = 8.284(\kappa\eta)^{4/3}+12.978(\kappa\eta)^2$, and the coefficients are $A_{\mathrm{T}} = 1.863\times 10^{-2}$, $A_{\mathrm{S}} = 1.9\times 10^{-4}$ and $A_{\mathrm{TS}} = 9.41\times 10^{-3}$.

Consequently, following the work of Pan *et al.*,[18] who derived the analytical expression of the effective oceanic turbulence strength under the Nikishov spectrum through the extended Huygens–Fresnel treatment, the equivalent temperature structure constant relation and related asymptotic approximations, the strength of oceanic turbulence G is given by

$$\begin{aligned} G &= 1.2765\times 10^{-8}\omega^{-2}\varepsilon^{-1/3}\eta^{-1/3}\chi_{\mathrm{T}} \\ &\quad \times\left(47.5708-17.6701\omega+6.78335\omega^2\right), \end{aligned} \quad (10)$$

and

$$\begin{aligned} &\langle \exp[\psi(\boldsymbol{\rho}_1,\boldsymbol{r}_1)+\psi^*(\boldsymbol{\rho}_2,\boldsymbol{r}_2)]\rangle \\ &= \exp\{-k^2 z G[(\boldsymbol{\rho}_1-\boldsymbol{\rho}_2)^2+(\boldsymbol{r}_1-\boldsymbol{r}_2) \\ &\quad \times(\boldsymbol{\rho}_1-\boldsymbol{\rho}_2)+(\boldsymbol{r}_1-\boldsymbol{r}_2)^2]\}, \end{aligned} \quad (11)$$

where the Kolmogorov microscale η describes the characteristic smallest scale eddies in oceanic turbulence. ε represents the dissipation rate of turbulent kinetic energy per unit mass, ranging from 10^{-1} $\mathrm{m^2/s^3}$ to 10^{-10} $\mathrm{m^2/s^3}$. χ_{T} is the dissipation rate of mean-squared temperature, varying between 10^{-4} $\mathrm{K^2/s}$ and 10^{-10} $\mathrm{K^2/s}$. The parameter ω defines the temperature–salinity contribution ratio ranging from -5 to 0, corresponding to a transition from temperature-dominant to salinity-dominant turbulence. These parameters affect beam propagation through their influence on the turbulence strength G in the adopted model. According to Eq. (10), within the specific oceanic turbulence spectrum adopted in this work, the strength of oceanic turbulence G increases with the increasing χ_{T} and decreasing ε and η.[27] It should be noted that these trends are valid within the framework of the adopted spectrum model, the associated derivation conditions, and the parameter ranges considered here.

Substituting Eq. (11) into Eq. (6), it can be obtained that

$$\begin{aligned} &W(\rho_1,\rho_2,\theta_1,\theta_2,z) \\ &= \left(\frac{k}{2\pi z}\right)^2 \int_0^{+\infty}\int_0^{+\infty}\int_0^{2\pi}\int_0^{2\pi} W(r_1,r_2,\phi_1,\phi_2,0) \\ &\quad \times \exp\left[-\frac{\mathrm{i}k}{2z}\left(\rho_1^2-2r_1\rho_1\cos(\phi_1-\theta_1)+r_1^2\right)\right] \\ &\quad \times \exp\left[\frac{\mathrm{i}k}{2z}\left(\rho_2^2-2r_2\rho_2\cos(\phi_2-\theta_2)+r_2^2\right)\right] \\ &\quad \times \exp\{-k^2 z G[(\boldsymbol{\rho}_1-\boldsymbol{\rho}_2)^2+(\boldsymbol{r}_1-\boldsymbol{r}_2) \\ &\quad \times(\boldsymbol{\rho}_1-\boldsymbol{\rho}_2)+(\boldsymbol{r}_1-\boldsymbol{r}_2)^2]\} \\ &\quad \times r_1 r_2 \mathrm{d}r_1 \mathrm{d}r_2 \mathrm{d}\phi_1 \mathrm{d}\phi_2. \end{aligned} \quad (12)$$

Assuming $\theta_1=\theta_2=\theta$ and $\rho_1=\rho_2=\rho$, the intensity can be written as

$$\begin{aligned} I(\rho,\theta,z) &= W(\rho_1=\rho_2=\rho,\theta_1=\theta_2=\theta,z) \\ &= \left(\frac{k}{2\pi z}\right)^2 \int_0^{+\infty}\int_0^{+\infty}\int_0^{2\pi}\int_0^{2\pi} W(r_1,r_2,\phi_1,\phi_2,0) \\ &\quad \times \exp\left[-\frac{\mathrm{i}k}{2z}\left(\rho^2-2r_1\rho\cos(\phi_1-\theta)+r_1^2\right)\right] \\ &\quad \times \exp\left[\frac{\mathrm{i}k}{2z}\left(\rho^2-2r_2\rho\cos(\phi_2-\theta)+r_2^2\right)\right] \\ &\quad \times \exp\left\{-k^2 z G\left[r_1^2-2r_1 r_2\cos(\phi_1-\varphi_2)+r_2^2\right]\right\} \\ &\quad \times r_1 r_2 \mathrm{d}r_1 \mathrm{d}r_2 \mathrm{d}\phi_1 \mathrm{d}\phi_2. \end{aligned} \quad (13)$$

The assumption $\theta_1=\theta_2=\theta$ and $\rho_1=\rho_2=\rho$ corresponds to evaluating the cross-spectral density at the same spatial point at the receiving plane. Equation (13) describes the intensity distribution of the windmill beam at the receiving plane after propagating through oceanic turbulence. The beam intensity distribution is jointly determined by the initial field distribution and the phase disruptions induced by oceanic turbulence.[5] The phase disruptions are characterized by the turbulence parameter G. As propagation distance increases or turbulence intensity intensifies, the term associated with G leads to intensity attenuation. From the theoretical derivation, it can be seen that oceanic turbulence mainly affects the beam intensity rather than completely destroying its fundamental structure.

3. Numerical simulations

Based on the above theoretical model, we investigate the propagation properties of windmill beams through oceanic turbulence by numerical simulations.

Firstly, we analyze the influences of beam parameter α on the propagation properties of windmill beams through oceanic turbulence by numerical simulations based on the theoretical model. Following the definition in Eq. (3), α describes the ellipticity of the windmill beam coordinate distribution. As shown in Fig. 1(a), for the double-leaf windmill beam, as α increases, the angle of the two leaves increases accordingly, accompanied by an increase in the leaf length and the coverage area. This trend indicates that α controls the transverse

geometry of the double-leaf pattern. The elliptic coordinate transformation introduces transverse scaling. As α increases, the beam profile gradually evolves from a pronounced elliptical distribution toward a more expanded transverse geometry. This leads to a wider angular coverage of each leaf. With increasing propagation distance, the windmill beam gradually expands and stretches due to diffraction and the effect of oceanic turbulence, while the fundamental double-leaf structure remains recognizable.

In addition, the size of the windmill leaves plays an important role in beam propagation through oceanic turbulence. Larger leaves, corresponding to increased leaf length and coverage area at higher values of α, interact with a broader turbulent region. Consequently, beams with larger leaf areas experience stronger phase distortions and intensity degradation during propagation. Overall, these results demonstrate that α offers an effective way to modulate windmill beams for underwater transmission. Since the three-leaf and four-leaf windmill beams are generated by rotating a single windmill phase distribution by multiple angles and superposing the corresponding fields, the choice of α directly affects the leaf separation and pattern overlap. Therefore, we set $\alpha = 30^\circ$ in the following simulations to obtain a clear and complete multi-leaf windmill structure. This choice also ensures that the individual leaves are well separated.

Unless otherwise specified, the numerical calculation parameters are adopted as follows: the beam waist radius is $w_0 = 2$ mm, the characteristic beam parameters are $a = 8 \times 10^6$, $b = 2$ and $\alpha = 30^\circ$, which correspond to the stretching extent, the radial power exponent, and the ellipticity of the windmill beam coordinate distribution, respectively. The Kolmogorov microscale is $\eta = 10^{-3}$ m; the rate of dissipation of turbulence kinetic energy per unit mass of fluid is $\varepsilon = 10^{-7}$ m^2/s^3; the dissipation rate of the mean-squared temperature is $\chi_T = 10^{-8}$ K^2/s and the temperature–salinity contribution ratio is $\omega = -2.5$. We performed the numerical calculations on a dual-channel 52-core (8272CL) server. Since the numerical integration requires substantial computational effort, parallel computing was employed in the simulations to improve efficiency.

We numerically simulated the propagation of multi-leaf windmill beams through oceanic turbulence as illustrated in Fig. 1(b). The generation of multi-leaf windmill beams is achieved by coherently superposing rotated copies of a fundamental windmill phase distribution at equal angular intervals. In general, an N-leaf windmill beam is produced by rotating the basic windmill phase distribution in steps of $360^\circ/N$ and coherently adding all N angular components. As shown in Figs. 1(b1)–1(b4), the single-leaf windmill beam exhibits a compact and concentrated leaf structure. As the propagation distance increases, the leaf expands outward while the leaf tips become more diffused. Between the two wings of each leaf, tiny spots are observed, which gradually dim as the radial distance from the beam center increases. Similarly, in Figs. 1(b5)–1(b8), the double-leaf windmill beam maintains a clearly identifiable two-leaf structure during propagation. With increasing distance, both leaves stretch and broaden, and the tiny spots along each leaf become more pronounced. For Figs. 1(b9)–1(b12) and 1(b13)–1(b16), the three-leaf and four-leaf windmill beams both display stable multi-leaf structures during propagation. As the distance increases, the leaves get wider and longer, and the central intersection region becomes broader. Moreover, we can see clearly that the windmill leaf does not exhibit perfect symmetry after propagation in oceanic turbulence. There are differences in intensity between the two wings of each leaf.

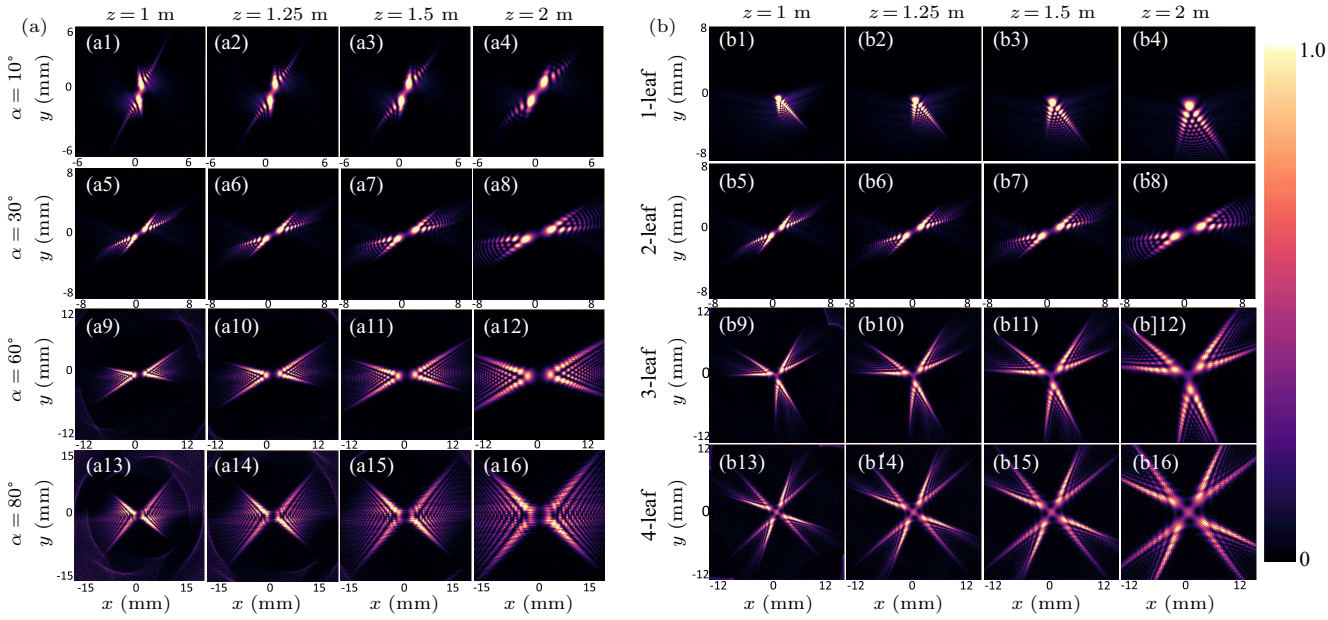

Fig. 1. (a) Numerical simulations of the propagation of windmill beams through oceanic turbulence for different values of the ellipticity parameter α. (a1)–(a4) $\alpha = 10^\circ$, (a5)–(a8) $\alpha = 30^\circ$, (a9)–(a12) $\alpha = 60^\circ$, (a13)–(a16) $\alpha = 80^\circ$. (b) Numerical simulations of the propagation of windmill beams through oceanic turbulence with different numbers of leaves. (b1)–(b4) 1-leaf, (b5)–(b8) 2-leaf, (b9)–(b12) 3-leaf, (b13)–(b16) 4-leaf.

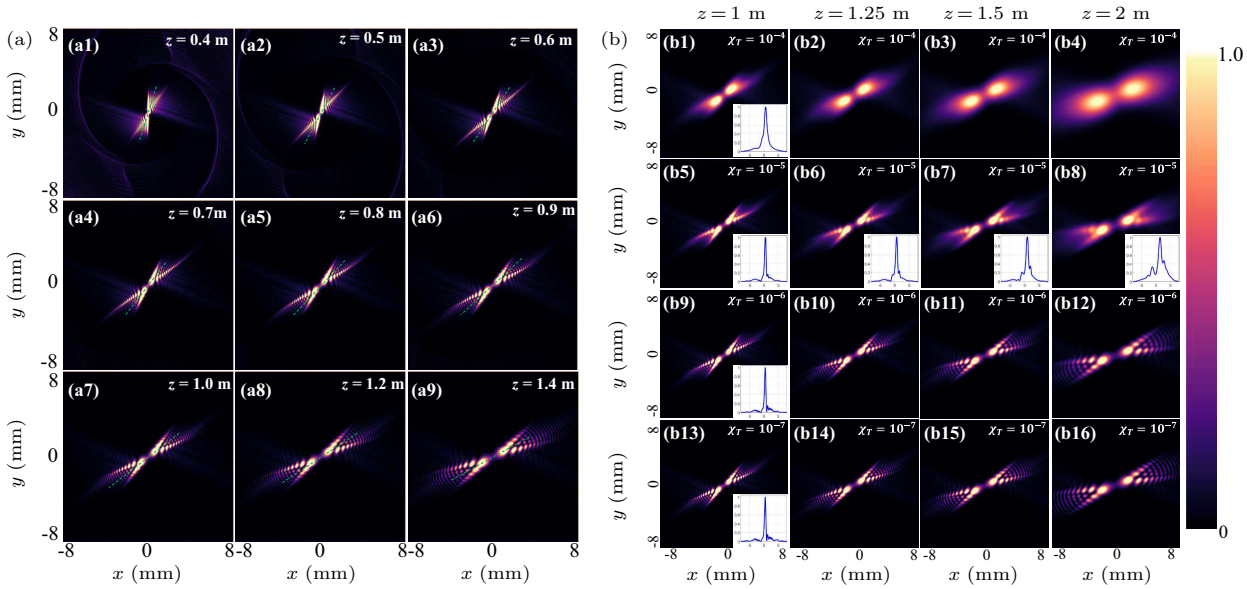

Fig. 2. (a) Self-rotation characteristics of the double-leaf windmill beam during propagation through oceanic turbulence. Panels (a1)–(a9) correspond to the propagation distance $z = 0.4$ m, 0.5 m, 0.6 m, 0.7 m, 0.8 m, 0.9 m, 1.0 m, 1.2 m and 1.4 m, respectively. (b) Propagation of the double-leaf windmill beam through oceanic turbulence for different values of χ_T. (b1)–(b4) $\chi_T = 10^{-4}$, (b5)–(b8) $\chi_T = 10^{-5}$, (b9)–(b12) $\chi_T = 10^{-6}$, (b13)–(b16) $\chi_T = 10^{-7}$.

Subsequently, we further investigate the dynamic transmission properties of windmill beams in oceanic turbulence. In the numerical simulations, we set $a = 8 \times 10^6$; in this case, the windmill beam rotates clockwise as the propagation distance increases. As shown in Fig. 2(a), each subfigure uses a dashed line to mark the direction along the main bright lobe. This reference line is used to determine whether the beam undergoes self-rotation during propagation. It can be seen that this self-rotation effect is more pronounced at shorter propagation distances. In addition, the rotation direction is determined by the sign of the stretching extent a; reversing its sign leads to self-rotation in the opposite (counterclockwise) direction. Therefore, as the propagation distance increases, the windmill beam not only expands and stretches but also exhibits self-rotation in oceanic turbulence.

Moreover, we investigate the dissipation rate of the mean-squared temperature χ_T. This parameter usually takes larger values in regions of strongly stratified water and energetic turbulence.[28] In Fig. 2(b), increasing χ_T causes the double-leaf windmill beam to diverge more strongly. As χ_T increases, the low-intensity gap separating the two leaves becomes blurred, indicating a gradual degradation of the structured profile. The normalized intensity profiles extracted along the transverse center line of each beam pattern are also shown in the lower-right corner of Figs. 2(b1), 2(b5), 2(b9), 2(b13) and 2(b5)–2(b8). Here, the beam width is defined as the full width at half maximum (FWHM) of the normalized intensity profile. For Figs. 2(b1), 2(b5), 2(b9), 2(b13) at $z = 1$ m, the beam width increases from 0.545 mm to 1.185 mm as χ_T increases. For Figs. 2(b5)–2(b8), with fixed χ_T, the beam width increases from 0.625 mm to 1.328 mm as the propagation distance z increases. It can be seen that the beam width grows with increasing χ_T and propagation distance z, while the beam contrast exhibits a decreasing trend. Within the adopted oceanic turbulence spectrum, a larger χ_T corresponds to a larger turbulence strength G, which enhances intensity fluctuations and accelerates the degradation of the windmill beam profile. Furthermore, the influence of χ_T becomes more evident at longer propagation distances, suggesting that the degradation is a cumulative effect rather than an instantaneous distortion.

When $\chi_T = 10^{-4}$, windmill beams propagating in such strong turbulence lose their structured features and degenerate into a Gaussian-like profile,[12,15,18] consistent with previous results for other structured beams in underwater oceanic turbulence.

4. Experiments

An experimental setup for windmill beams propagating through oceanic turbulence was established to verify the numerical simulations. The experimental schematic diagram for generating the windmill beams is shown in Fig. 3(a). A laser with a wavelength of 632.8 nm was used as the light source. After beam expansion and collimation, the light passed through a circular aperture, which was used to reduce stray light and suppress unwanted interference. Then the beam propagated through a linear polarizer to adjust beam intensity before being incident on a reflective phase-only spatial light modulator (SLM, XinGuang, model I-101; pixel pitch of 6 μm; pixel number of 1920×1080). After modulation by the SLM, the beam entered a turbulence simulator (1.2 m×0.3 m×0.3 m). The received beam intensity patterns were recorded by a CMOS camera (JAI, GOX-2402-PGE,

pixel pitch of 3.45 μm, pixel number of 1920 × 1200). A water pump (maximum power of 8 W, maximum head of 1 m, maximum flow rate 450 L/h, and an outlet diameter of 12 mm) was used to generate flow disturbance in the turbulence simulator. In the experiment, two laboratory conditions were considered: static water (pump off) and turbulence (pump on at 8 W). In addition, different salinity conditions were simulated by varying the mass fraction of salt in the water. In this work, turbulence was generated by pump-driven flow disturbance and treated as a laboratory operating condition. Compared with the static condition (pump off), the turbulence condition (pump on) leads to more pronounced beam spreading and degradation, and this effect becomes more significant with increasing salinity, which is consistent with the Nikishov-spectrum-based theoretical model in terms of trend behavior.

The water temperature was maintained at approximately 23 °C. Before each experiment, all optical components were aligned along a common optical axis. The experimental results for the four-leaf windmill beam are presented in Fig. 3(b), while the results for the single-, double-, and three-leaf windmill beams are shown in Fig. 3(c). Compared with the static condition, turbulent conditions lead to weakening of the outer leaves of the windmill beams, together with noticeable structural degradation. These effects become more pronounced with increasing salinity level. Meanwhile, the original rotational symmetry is partially broken. Despite these distortions, the overall featured structure of the windmill beams remains distinguishable under turbulent conditions across varying salinity levels, suggesting the stability of the windmill beams through oceanic turbulence.

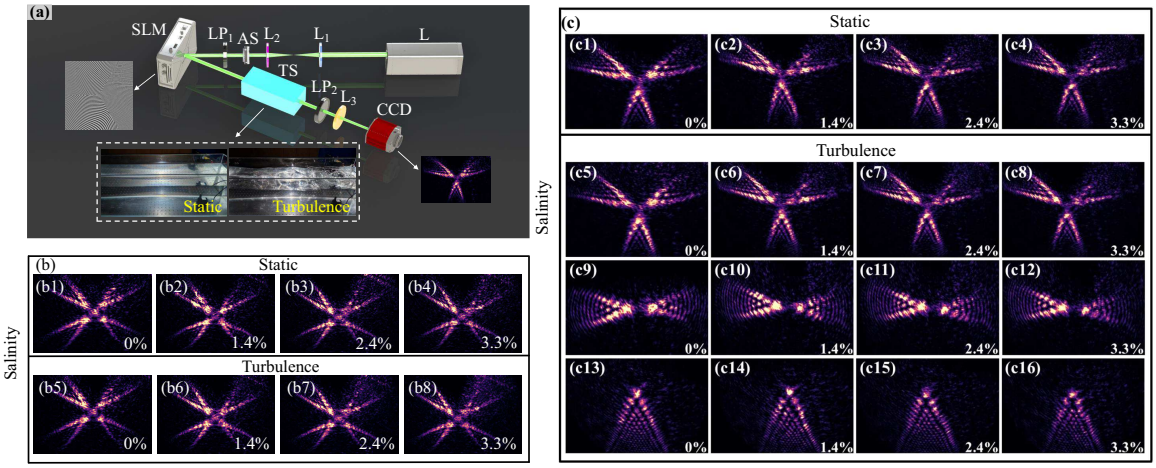

Fig. 3. (a) Experimental schematic diagram for the generation of windmill beams. (L: laser; L_1–L_3: convex lens; AS: aperture; LP_1: linear polarizer; SLM: spatial light modulator; TS: a 1.2 m-long turbulence simulator; from left to right: static water and turbulence; LP_2: linear polarizer; CCD: charge-coupled device). (b) Four-leaf windmill beams under static and turbulent conditions at different salinity levels. (c) Single-, double-, and three-leaf windmill beams under static and turbulent condition at different salinity levels. From left to right, the mass fraction of salt is 0%, 1.4%, 2.4% and 3.3%, respectively.

5. Encoding and decoding based on windmill array beams

Since double-leaf, three-leaf, and four-leaf windmill beams can be constructed by the coherent superposition of equally rotated copies of a single windmill phase distribution, distinct windmill modes with different spatial structures can be generated. These modes exhibit good mutual distinguishability. By encoding information through the number of leaves, different windmill beam states can be constructed and distinguished for optical encoding and decoding. In this work, the windmill beam leaf number is used to encode digital information. The single-, double-, three-, and four-leaf windmill beams are mapped to the binary states 00, 01, 10 and 11, respectively. Figure 4(a) illustrates the mapping between windmill beam states and corresponding 2-bit symbols. To organize the data sequence, the detection plane is divided into four regions (regions 1–4), as shown in Fig. 4(b). An example of the encoded frame is presented in Fig. 4(c), where windmill beam states are assigned to the corresponding regions. The resulting region-based bit sequence is summarized in Fig. 4(d). This encoding scheme provides a clear mapping between beam states and binary symbols, which supports reliable decoding of the encoded information.

As shown in Fig. 5, a convolutional neural network (CNN) classifier is employed to identify the number of leaves carried by the received windmill beams. The classifier is based on a ConvNeXt-Tiny architecture with ImageNet-pretrained weights, where the backbone is frozen and only the classification head is fine-tuned for four classes. The dataset consists of 1506 images and is randomly divided into training, validation, and test sets with a ratio of 8:1:1 using a fixed random seed of 42. The model is trained using the Adam optimizer, and standard preprocessing and data augmentation are applied. Both experimental and simulated beam images are used for training and evaluation. The preprocessed images are fed into the CNN for feature extraction and classification, and the predicted class

is then used to determine the leaf number and decode the encoded binary information.

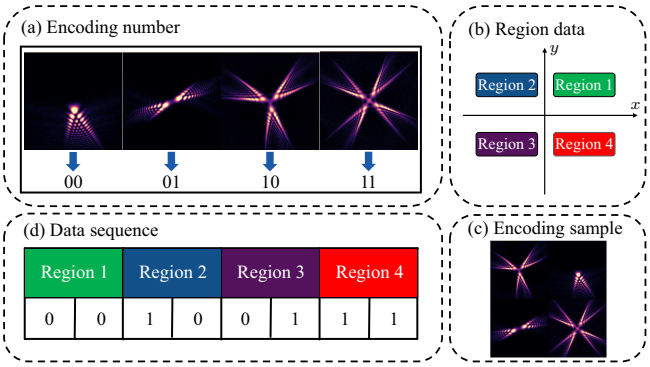

Fig. 4. Encoding scheme for windmill-beam-based information modulation. (a) Mapping between the windmill-beam leaf number and the corresponding 2-bit symbols (00, 01, 10, and 11). (b) Division of the detection plane into four regions (regions 1–4) for data organization. (c) A sample of an encoded frame formed by windmill beams with different leaf numbers. (d) Region-based bit sequence corresponding to the encoded frame sample.

The decoding performance of the proposed method is evaluated as follows. Under turbulent conditions, Fig. 5(b) presents the classification confidence of windmill beams with different leaf numbers across varying salinity levels. The orange, blue, green, and red curves correspond to one-leaf, double-leaf, three-leaf, and four-leaf beams, respectively.

All curves exhibit a gradual decrease in confidence as salinity increases. However, no misclassification is observed for the tested experimental samples. Under turbulent and high salinity conditions, the CNN maintains classification confidence above 98.0% for all leaf numbers. Figure 5(c) shows the average classification confidence for each leaf class under pump-induced turbulence and different salinity levels, where SEM denotes the standard error of the means. The average confidence for all four classes exceeds 98.8%, with small standard errors, indicating stable predictions. These results demonstrate that the model can reliably distinguish windmill beam states encoded by different leaf numbers under the experimental conditions considered in this work. The high classification confidence is closely related to the stability of the windmill beam encoding. The discrete leaf structure provides physically distinguishable features. Moreover, the corresponding windmill beam states with different leaf numbers are well separated and easily distinguishable. These characteristics remain largely preserved even under turbulent conditions and salinity-induced distortions.

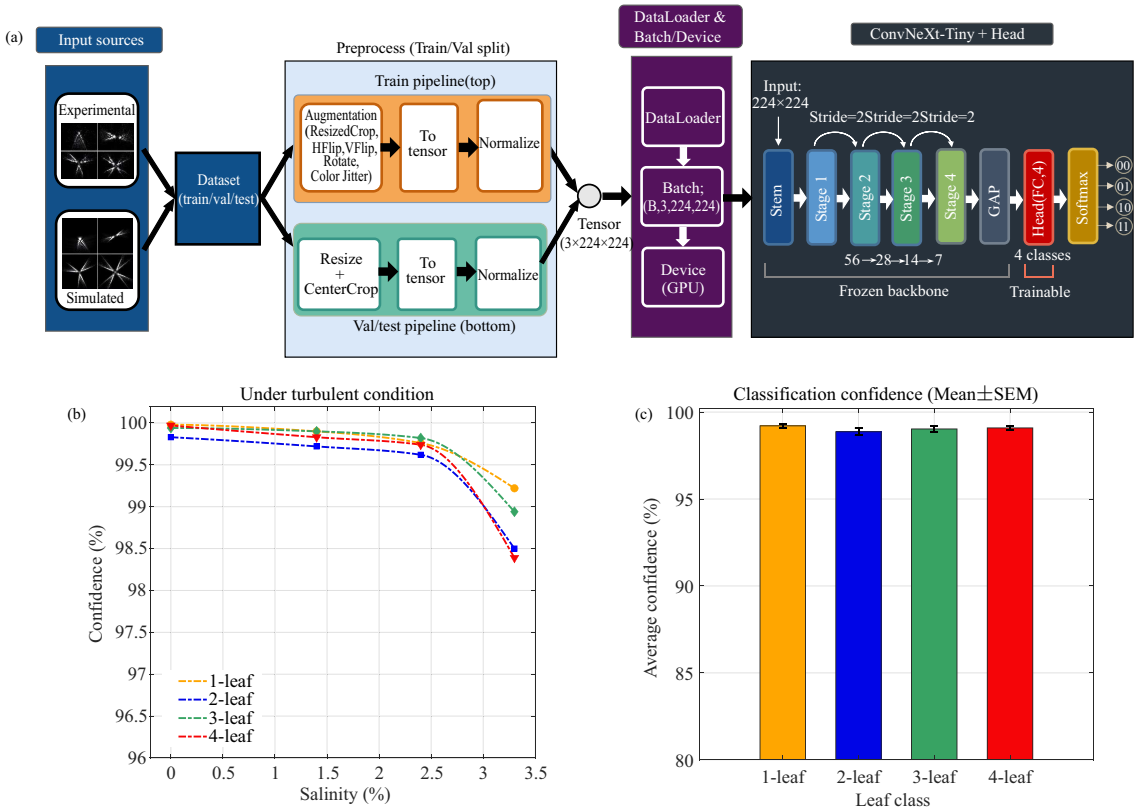

Fig. 5. (a) The CNN workflow for windmill-beam decoding. (b) CNN classification confidence of windmill beams with different leaf numbers under turbulent condition with varying salinity levels. (c) Average classification confidence of windmill beams with different leaf numbers under turbulent condition and varying salinity levels.

We carried out an experiment for windmill array beams propagating through oceanic turbulence to validate the feasibility of the encoding and decoding scheme based on windmill array beams. As shown in Fig. 6(a), we generated the windmill array beams using a phase synthesis method.[29] Let $\varphi_k(x,y)$ represent the phase of the k-th channel ($k = 1, 2, 3, 4$). The specific mode for each channel can be selected from one-leaf, double-leaf, three-leaf and four-leaf arbitrarily. To

separate these beams spatially at the receiving plane, we applied a specific linear phase term to each channel. The final synthetic phase is calculated by

$$\Phi(x,y) = \sum_{k=1}^{4} \varphi_k(x,y) \cdot \exp\left[\mathrm{i}2\pi S\left(p_k x + q_k y\right)\right]. \tag{14}$$

The parameter S controls the separation distance between the array elements. Parameters p_k and q_k are the phase shift factors in the x and y directions, respectively. We can use the phase shift factors to adjust the position of each windmill beam in the beam array.

In the experiment, we selected the turbulent condition at a salt mass fraction of 3.3%. As shown in Fig. 6(b), it can be seen that under such experimental conditions, the structure of each windmill beam was affected to varying degrees by oceanic turbulence, resulting in intensity attenuation and phase distortion. To minimize the impact of oceanic turbulence on the edges of each windmill beam, the spacing between each windmill beam should be as close as possible while ensuring separation. Furthermore, compared to one-leaf windmill beams, multi-leaf beams are more susceptible to oceanic turbulence, exhibiting more pronounced structural degradation. The results in Fig. 6(b) indicate that the experimental results match well with the numerical simulations. Despite varying degrees of structural degradation observed in the experimental beam arrays, they could still be accurately identified and classified by the above-mentioned CNN model. This validates the feasibility and stability of the encoding and decoding scheme based on windmill array beams in oceanic turbulence.

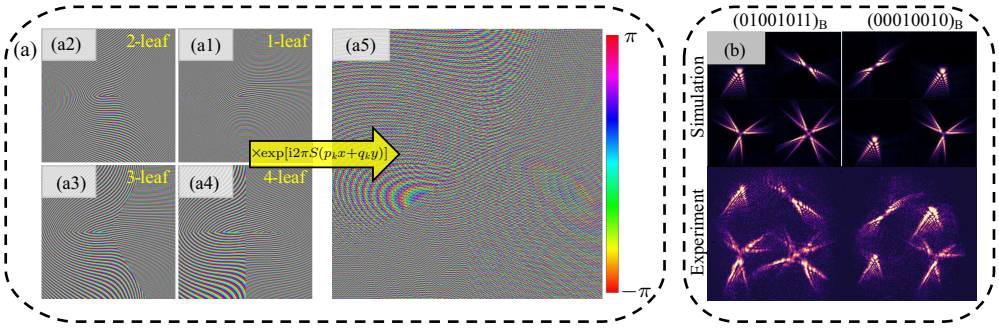

Fig. 6. (a) Schematic illustration of the phase synthesis. (a1)–(a4) Phase distributions of the windmill beams with one-leaf, double-leaf, three-leaf, and four-leaf structures, respectively. (a5) Synthesized phase distribution. (b) Simulated and experimentally captured intensity distributions of the windmill beam arrays corresponding to the binary sequences $(01001011)_{\mathrm{B}}$ and $(00010010)_{\mathrm{B}}$.

6. Conclusion

In summary, we explored the propagation characteristics and communication potential of windmill array beams in oceanic turbulence. By using the extended Huygens–Fresnel principle and Nikishov's spectrum, we employed a theoretical model to show how these beams maintain their multi-leaf shapes during underwater transmission. Based on this model, our numerical simulations provide a parametric analysis and evaluate the propagation behaviors of windmill beams in oceanic turbulence. Besides that, our laboratory experiments in a 1.2 m turbulence simulator confirm that windmill beams are stable under turbulent conditions and varying salinity levels. Beams keep their basic features under these experimental conditions. Accordingly, based on these distinguishable structures, we proposed an encoding scheme that maps the number of leaves to 2-bit symbols. By employing a CNN for decoding, we successfully identified the different beam states and achieved high accuracy despite the oceanic turbulence distortions. These results demonstrate that windmill beams combined with deep learning offer a reliable and effective way to enhance the performance of underwater wireless optical communication systems.

Data availability statement

The data that support the findings of this study will be made available on request.

Acknowledgement

Project supported by the National Natural Science Foundation of China (Grant No. 62575141).

References

[1] Sun K, Li Y and Han Z 2024 *Appl. Sci.* **14** 206
[2] Liu A, Yuan Y, Yin H, Zhao H and Fu X 2023 *J. Mar. Sci. Eng.* **11** 253
[3] Cai C, Du Z, Liao W, He Y, Ma X, Qin S, Wang R, Wang X, Zhang T, Song G, Chen Q, Zhang Y, Gao Y, Wang H, Zhang Z and Xu J 2024 *J. Lightwave Technol.* **42** 8541
[4] Chen D, Li J, Zhou Y and Dong K 2025 *Appl. Opt.* **64** 8425
[5] Korotkova O 2019 *Prog. Opt.* **64** 1
[6] Baykal Y, Ata Y and Gokçe M C 2022 *Opt. Laser Technol.* **156** 108624
[7] Sun Z C, Yan M Y and Xu B J 2020 *Chin. Phys. B* **29** 104101
[8] Chen X P, Xu C J, Yang Q, Luo Z M, Li X X and Deng D M 2020 *Chin. Phys. B* **29** 064202
[9] Janet C A P, Rajesh K B, Udhayakumar M, Jaroszewicz Z and Pillai T V S 2016 *Chin. Phys. Lett.* **33** 124206
[10] Sundaram C M, Prabakaran K, Anbarasan P M, Rajesh K B and Musthafa A M 2016 *Chin. Phys. Lett.* **33** 064203
[11] Zhu Y F and Geng T 2020 *Acta Phys. Sin.* **69** 014205 (in Chinese)
[12] Cong R, Liu D, Yin Y, Zhong H, Wang Y and Wang G 2025 *Phys. Lett. A* **545** 130513
[13] Li Y, Cui Z, Han Y and Hui Y 2019 *J. Opt. Soc. Am. A* **36** 471

[14] Chang H, Yin X, Cui X, Chen X Z, Su Y Z, Ma J X, Wang Y J, Zhang L and Xin X 2019 *Appl. Opt.* **58** 6085
[15] Chen L, Liu D, Gao H, Dong A and Wang Y 2025 *Opt. Laser Technol.* **190** 113264
[16] Zhao S, Zhang W, Wang L, Li W, Gong L, Cheng W, Chen H and Gruska J 2019 *Sci. Rep.* **9** 2025
[17] Wang X, Yang Z and Zhao S 2019 *Optik* **176** 49
[18] Pan Y, Zhao M, Zhang M, Dou J, Zhao J, Li B and Hu Y 2023 *Opt. Laser Technol.* **159** 109024
[19] Liu D J, Wang Y C, Zhong H Y, Wang G Q, Yin H M and Dong A Y 2019 *Opt. Laser Technol.* **119** 105604
[20] Shen D H, Wang K and Zhao D M 2019 *Opt. Express* **27** 24642
[21] Prabakaran K, Rajesh K B, Sumathira S, Bharathi M D, Hemamalini R, Musthafa A M and Aroulmoji V 2016 *Chin. Phys. Lett.* **33** 094203
[22] Zhan Q W 2006 *Opt. Lett.* **31** 867
[23] Niu K, Wan L and Tang D 2024 *Opt. Lett.* **49** 6888
[24] Niu K, Liu Y, Chu Z, Tian Q, He X, Pan C and Wang F 2023 *Opt. Express* **31** 12150
[25] Song Y S, Dong K Y, Chang S, Dong Y and Zhang L 2020 *Chin. Phys. B* **29** 064213
[26] Wolf E 2003 *Phys. Lett. A* **312** 263
[27] Huang Y, Zhang B, Gao Z, Zhao G and Duan Z 2014 *Opt. Express* **22** 17723
[28] Thorpe S A 2007 *An Introduction to Ocean Turbulence* 1st ed. (Cambridge: Cambridge University Press) pp. 1–266
[29] Yang W, Shan S, Liu M, Cheng S, Shui T, Dai C and Tao S 2025 *Opt. Express* **33** 28808